ChemPubSoc Europe

DOI: 10.1002/chem.201503356

CHEMISTRY A European Journal Full Paper

Lithium-Ion Batteries

Mesoporous Carbon Nanofibers Embedded with MoS_2 Nanocrystals for Extraordinary Li-Ion Storage

Shan Hu,[a, b] Wen Chen,*[a] Evan Uchaker,[b] Jing Zhou,[a] and Guozhong Cao*[b, c]

Abstract: MoS_2 nanocrystals embedded in mesoporous carbon nanofibers are synthesized through an electrospinning process followed by calcination. The resultant nanofibers are 100–150 nm in diameter and constructed from MoS_2 nanocrystals with a lateral diameter of around 7 nm with specific surface areas of 135.9 $m^2 g^{-1}$. The MoS_2@C nanofibers are treated at 450 °C in H_2 and comparison samples annealed at 800 °C in N_2. The heat treatments are designed to achieve good crystallinity and desired mesoporous microstructure, resulting in enhanced electrochemical performance. The small amount of oxygen in the nanofibers annealed in H_2 contributes to obtaining a lower internal resistance, and thus, improving the conductivity. The results show that the nanofibers obtained at 450 °C in H_2 deliver an extraordinary capacity of 1022 mA h g^{-1} and improved cyclic stability, with only 2.3% capacity loss after 165 cycles at a current density of 100 mA g^{-1}, as well as an outstanding rate capability. The greatly improved kinetics and cycling stability of the mesoporous MoS_2@C nanofibers can be attributed to the crosslinked conductive carbon nanofibers, the large specific surface area, the good crystallinity of MoS_2, and the robust mesoporous microstructure. The resulting nanofiber electrodes, with short mass- and charge-transport pathways, improved electrical conductivity, and large contact area exposed to electrolyte, permitting fast diffusional flux of Li ions, explains the improved kinetics of the interfacial charge-transfer reaction and the diffusivity of the MoS_2@C mesoporous nanofibers. It is believed that the integration of MoS_2 nanocrystals and mesoporous carbon nanofibers may have a synergistic effect, giving a promising anode, and widening the applicability range into high performance and mass production in the Li-ion battery market.

1. Introduction

There is increasing demand for the development of clean energy-storage devices for applications in portable electronics, electric vehicles (EVs), and hybrid electric vehicles (HEVs), which must have the advantages of high power density, high energy density, and high safety.[1] Lithium-ion batteries (LIBs) have dominated energy-storage technologies and power-source markets because of their high energy density, high voltage, and long lifespan, which are desirable features for large-scale energy applications.[2] Currently, numerous research efforts are aimed at designing electrode materials with nanostructured architectures to achieve high-performance LIBs. Among various nanostructured materials, considerable interest has been directed to 1D nanostructures such as nanowires, nanotubes, nanorods, and nanofibers as promising electrode materials for LIBs. In general, the advantages of 1D nanomaterials are: 1) their large specific surface area between the active materials and electrolyte, which increases surface/interface storage; 2) a short diffusion length for Li ions, which gives rise to a high-rate charge/discharge capability; and 3) their ability to absorb a large volume expansion, which leads to stable cycle performance.[3] However, there also are some disadvantages of 1D nanomaterials, such as low energy density and self-aggregation, which may block the electron/Li-ion transport.[4]Specially designed nanostructures should be considered to address these problems. Mesoporous nanostructured materials, which possess a large specific surface area and exhibit the intrinsic nanomaterial nature of self-aggregation, have been desirable structures allowing efficient contact with the electrolyte and fast Li-ion transport, leading to improved LIB electrochemical performance. For example, mesoporous V_2O_5 nanofibers exhibited a high discharge capacity of 370 mA h g^{-1}, and a high rate capability at 800 mA g^{-1} with little cyclic degradation.[5] Mesoporous graphene-based TiO_2/SnO_2 nanosheets with a large surface area of 138 $m^2 g^{-1}$ and large pore volume (0.133 $cm^3 g^{-1}$), synthesized through a facile and scalable stepwise method, could effectively accommodate the volume change and shorten the transport lengths for Li ions and electrons, and presented a reversible capacity of 600 mA h g^{-1} for

[a] Dr. S. Hu, Prof. W. Chen, Prof. J. Zhou
State Key Laboratory of Advanced Technology for Materials Synthesis and Processing, School of Materials Science and Engineering
Wuhan University of Technology, Wuhan, 430070 (P. R. China)
Fax: (+86)27-87760129
E-mail: chenw@whut.edu.cn

[b] Dr. S. Hu, Dr. E. Uchaker, Prof. G. Cao
Department of Materials Science and Engineering
University of Washington, Seattle, Washington, 98195 (USA)
E-mail: gzcao@u.washington.edu

[c] Prof. G. Cao
Beijing Institute of Nanoenergy and Nanosystems
Chinese Academy of Sciences, Beijing 100083 (P. R. China)

Supporting information for this article is available on the WWW under http://dx.doi.org/10.1002/chem.201503356.

over 300 cycles.[6] Therefore, mesoporous nanostructured materials are of particular interest as electrodes owing to their large surface areas, structural integrity, and effective mechanical support and void space to mitigate volume expansion, which make them a rational nanoarchitecture for LIB anode/cathode materials.

In recent years, a variety of preparation methods have been developed to obtain mesoporous nanostructured materials. The hard-template approach is very common for the fabrication of mesoporous nanostructured materials. Shen et al. successfully prepared mesoporous $Li_4Ti_5O_{12}$/C nanocomposites through a nanocasting technique, using CMK-3 as the hard template.[7] However, this process requires severe and costly reaction conditions. Subsequently, solution-based routes and electrodeposition methods for the synthesis of mesoporous nanostructured materials were introduced.[8] These methods are easily accessible, but scale-up for mass production is still challenging. Electrospinning, a versatile, facile, and economical method, can be applied to the large-scale synthesis of nanostructured materials.[9] In addition, electrospinning can generate mass-controllable 1D nanostructures and sophisticated architectures, and does not require complex technology.

A typical layered transition metal sulfide, MoS_2, which consists of Mo atoms sandwiched between two layers of closely packed S atoms, is the focus of much attention as an anode material for application in LIBs. It is an inorganic analogue of the graphene layered structure, in which the 2D molecular layers are weakly linked by van der Waals interactions. The weak van der Waals forces allow a fast diffusion path for the movement of Li ions without a significant increase in volume.[10] The special S-Mo-S layered structure enables expeditious Li-ion insertion/extraction during the discharge/charge process. Theoretically, MoS_2 can store four moles of Li ions on the basis of a redox conversion reaction, in which the MoS_2 is reduced to Mo nanocrystals dispersed in a Li_2S matrix upon lithiation, and is then reversibly restored to the corresponding disulfide after delithiation, leading to a capacity 3.5 times greater than that of commercial graphite anodes ($372\ mA\,h\,g^{-1}$). However, a key limiting factor in employing MoS_2-based anodes is their low energy density, which is attributed to the relatively narrow voltage window. Various nanostructured MoS_2 materials have been fabricated, which is an effective way to shorten the Li-ion diffusion pathway, and thus, to improve the rate performance compared with their "micro" MoS_2 counterparts.[11] There is further interest in the synthesis of MoS_2-carbon hybrids because carbon modification has the potential to enhance the electrical conductivity of the whole system, thereby giving a high reversible capacity and good cycling stability.[12]

In terms of integration of the above possible improving routes, the MoS_2-carbon nanostructured materials synthesized through a convenient and versatile electrospinning method could be one of the most favorable architectures as the anode of high-performance LIBs. So far, there are two publications concerning this field. Single-layered nanoplates of MoS_2 embedded in thin carbon nanowires by electrospinning obtained a high capacity of $661\ mA\,h\,g^{-1}$ after 1000 cycles.[13] Thin MoS_2 nanoflakes embedded in carbon nanofibers synthesized through a hydrothermal method combined with electrospinning and carbonization exhibited a reversible capacity of approximately $350\ mA\,h\,g^{-1}$ at a high current density of $1000\ mA\,g^{-1}$.[14] In our work, electrospinning has been adopted for the controllable fabrication of MoS_2 nanocrystals embedded in mesoporous carbon nanofibers to generate functional material mats as anodes for LIBs. Furthermore, among carbonaceous materials, carbon nanofibers have a good diffusion coefficient ($\approx 2\times10^{-7}\ cm^2\,s^{-1}$),[15] which is a critical parameter determining the power density of the Li-ion battery. Compared with our previous studies on flower-like C@MoS_2 composites obtained through the hydrothermal method,[10a] we have fabricated MoS_2@C mesoporous nanofibers successfully through electrospinning with low-cost and accessible raw materials, which may be of benefit for the application of LIBs in industrial production. In addition, our results demonstrate that MoS_2@C mesoporous nanofibers with improved interfacial charge-transfer kinetics and a robust microstructure exhibit high reversible capacities and excellent cycling stability upon evaluation as anode materials for LIBs.

2. Experimental Section

2.1 Materials synthesis

Poly(vinyl alcohol) (PVA, $M_w = 67000$ Sigma-Aldrich Co., Ltd., USA), ammonium tetrathiomolybdate (ATTM, Alfa Aesar Co., Ltd., USA), and dimethyl sulfoxide (DMSO, Alfa Aesar Co., Ltd., USA) were used without further purification. Aqueous PVA solution (15 wt%) was first prepared by dissolving the PVA in deionized water at 90 °C, and stirring for 3 h. The concentration of ATTM in DMSO was set to be $0.33\ g\,mL^{-1}$ and the solution was stirred at room temperature for 30 min. The above PVA was added into the precursor solution and stirred until a homogeneous reddish-brown solution was obtained. The weight ratio of PVA to ATTM was 1.05. The precursor solution was then transferred into a 3 mL plastic syringe with a stainless steel needle and driven by a syringe pump at a constant flow rate of $0.15\ mL\,h^{-1}$. The needle was connected to a high-voltage power supply (ES40P-5W, Gamma High Voltage, Inc.), with the voltage set to be approximately 20 kV. A piece of aluminum foil collector was grounded, with a distance of around 15 cm between the collector and the tip of the needle. The ATTM/PVA nanofibers were generated and formed flexible mats, which were then dried at 80 °C to evaporate the solvent. Afterwards, the nanofibers were annealed in a conventional tube furnace at 450 °C in H_2 for the reduction of ATTM to obtain good crystallinity with subsequent heat treatment under N_2 at 800 °C for 3 h to carbonize the PVA; the product was designated as MNF450. For comparison, the ATTM/PVA nanofibers were annealed at 800 °C in N_2 for 3 h, with the resulting material designated as MNF800.

2.2 Materials characterization

The crystal structure of the obtained samples was characterized by X-ray diffraction (XRD, D8 Bruker X-ray diffractometer with CuK_α radiation ($\lambda = 1.5418$ Å)). The morphology and composition of the sample were examined by using scanning electron microscopy (SEM, JEOL JSM-7000F) and energy-dispersive X-ray spectroscopy (EDX). Transmission electron microscopy (TEM) was performed with an FEI, Tecnai G2 F20 transmission electron microscope operating

at 200 kV accelerating voltage. The Brunauer–Emmett–Teller (BET) specific surface areas and pore size distributions were measured with a QuantaChrome NOVA 4200e analyzer. Thermogravimetric analysis (TGA) was performed on a TG instrument (NET ZSCH STA 409C). X-ray photoelectron spectroscopy (XPS) analysis was performed with a VG Multilab 2000 with AlK_α as the X-ray source.

2.3 Electrochemical measurement

For evaluation of the electrochemical performance, coin-type half-cells were assembled using the as-prepared nanofibers as anode materials for Li-ion batteries. The as-prepared active material was prepared by mixing the as-synthesized MoS_2@C nanofibers, Super P conductive carbon (TIMCAL Graphite & Carbon), and poly(vinylidene fluoride) (PVDF, Sigma-Aldrich) binder dispersed in N-methyl-2-pyrrolidone (NMP, Alfa Aesar) solution in a weight ratio of 80:10:10, respectively. The as-prepared active material slurry was spread uniformly onto Cu foil and dried in a vacuum oven at 80 °C overnight prior to coin-cell assembly. The electrochemical experiments were performed using CR2016-type coin cells, which were assembled in an argon-filled dry glovebox (Innovative Technology, IL-2GB) with MoS_2@C nanofibers as the working electrode, pure Li foil as the counter and reference electrodes, polypropylene membrane film as the separator, and 1 M $LiPF_6$ in ethylene carbon (EC)/dimethyl carbonate (DMC) as the electrolyte. Galvanostatic discharge and charge measurements were performed under different current densities in the voltage range 0.01–3.0 V at room temperature. Cyclic voltammetry (CV) was conducted on an electrochemical analyzer (CH Instruments, model 605C) in the voltage range 0.01–3.0 V (vs. Li/Li^+) at a scan rate of 0.2 mV s^{-1}. Electrochemical impedance spectroscopy (EIS) was recorded by applying the Solartron 1287A in conjunction with a Solartron 1260FRA/impedance analyzer with an amplitude of 5.0 mV in the frequency range 100 kHz to 0.01 Hz. The half-cells were tested at various current rates on the basis of the weight of the active material alone.

3. Results and Discussion

Figure 1 shows a schematic illustration of the fabrication of mesoporous MoS_2@C nanofibers. First, ATTM and PVA powders were dissolved in DMSO with continuous stirring to generate ATTM/PVA gel. Then, the gel was transferred to a syringe with the flow rate of the gel precursor set to about 0.15 mL h^{-1} to form ATTM/PVA fibers. After electrospinning and a short post-annealing procedure, the ATTM/PVA was transformed into MoS_2 nanocrystals to form mesoporous MoS_2@C nanofibers.

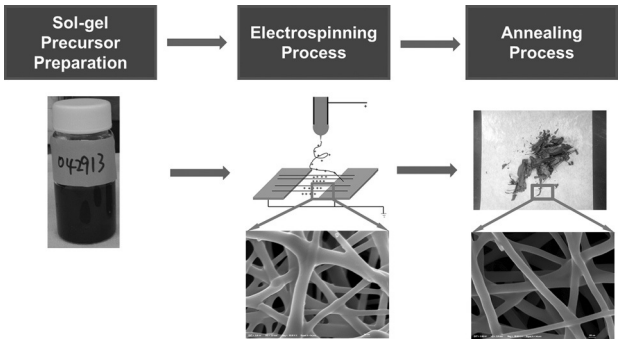

Figure 1. Schematic illustration of the fabrication of mesoporous MoS_2@C nanofibers.

This electrospinning method is conceptually straightforward, simple, and generic, as used in the fabrication of CoO-carbon and mesoporous V_2O_5 nanofibers.[5,16]

Figure 2a shows SEM images of the ATTM/PVA nanofibers; they are randomly oriented with smooth surfaces, and their lengths are more than tens of micrometers. The high-magnification image in Figure 2b demonstrates that the diameters of the nanofibers are distributed in the range 150–220 nm. With

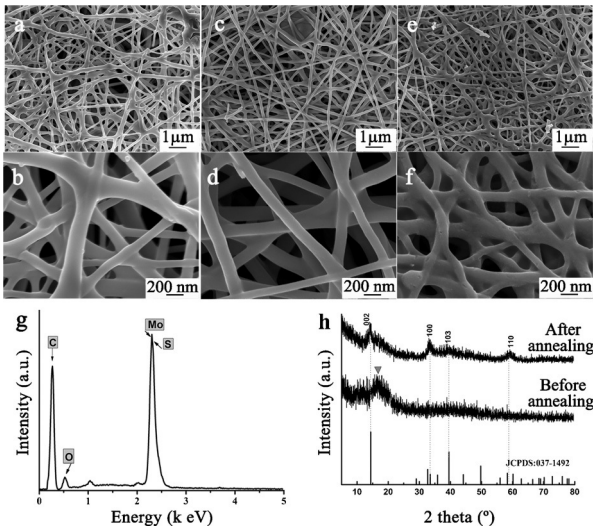

Figure 2. a,b) SEM images of as-prepared ATTM/PVA nanofiber; c,d) SEM images of MNF450; e,f) SEM images of MNF 800; g) EDX spectrum of MNF450; h) XRD patterns of MNF450 nanofibers before and after heat treatment.

the different calcination processes, however, new features started to evolve on the surface; the resulting morphology of the nanofibers was dependent on the calcination conditions. After heat treatment at 450 °C in H_2 and at 800 °C in N_2, orange nanofibers were transformed to black ones with a clear reduction in diameter from approximately 220 to around 130 nm (as shown in Figure 2c and 2d). No fracture of the nanofibers was observed after the heat treatment. The MoS_2@C nanofibers (named MNF450) were uniform, smooth, and consistent in toughness. The decreased diameter of the nanofibers could be attributed to pyrolysis, reduction, and carbonization of PVA and ATTM. The images of the MoS_2@C nanofibers (named MNF800) in Figure 2e demonstrate that the nanofiber morphology was conserved. Figure 2f, however, shows that the surface of the nanofibers became rough and their diameter was around 150 nm. It was also found that there were many pores in the fibers, which were composed of interconnected MoS_2 nanoplates. EDX was used to characterize the elemental compositions of the nanofibers for MNF450, as shown in Figure 2g. The EDX measurements confirmed the coexistence of Mo, S, C, and O elements with no detectable impurities, indicating that the nanofibers were made mainly of MoS_2. The elemental compositions of MNF450 and MNF800 are shown in Table 1. The calculated atomic ratios of S to Mo for MNF450 and MNF800 are 2.16 and 2.18, respectively, which are close to

Table 1. Elemental composition of the MoS_2@C nanofibers.

Elemental composition of the MoS_2@C nanofibers determined using EDX						
Composition	Mo [wt%]	S [wt%]	C [wt%]	O [wt%]	MoS_2 [wt%]	S/Mo ratio
MNF450	22.01	10.15	64.26	3.58	32.16	2.16
MNF800	16.86	12.29	59.52	10.90	29.15	2.18

the stoichiometry of MoS_2. The carbon component emanates from the carbonization of PVA, and a small amount of oxygen is attributed to the incomplete decomposition of PVA and partially oxidized Mo. More importantly, it is shown clearly that the oxygen mass fraction in MNF450 is 3.58 wt%, which is three times smaller than that of MNF800 (10.90 wt%). It can be explained that H_2 heat treatment is helpful to remove the residual oxygen. XRD analysis was performed to determine the phase information and crystallinity of the MNF450 sample before and after heat treatment. As shown in Figure 1h, there is a clear structural change from hydrous ammonium tetrathiomolybdate to hexagonal MoS_2. In detail, the XRD pattern of the as-electrospun MoS_2 nanofibers before annealing has a broad peak around 17°, which could be assigned to the hydrous ammonium tetrathiomolybdate, as reported in the literature.[13,17] There is clearly a large area of noise peaks, indicating the amorphous phase of the nanofibers before annealing. The lower intensities of diffraction peaks also confirmed the low crystallinity. After annealing, the nanofibers showed a different XRD pattern. All the diffraction peaks of the nanofibers can be indexed to the hexagonal MoS_2 phase with lattice parameters $a=3.16$, $b=3.16$, $c=12.30$ Å, and $\beta=90.00°$, which are in good agreement with the literature values (JCPDS: 00-037-1492). The interlayer space and grain size of the hexagonal MoS_2 were estimated using the Bragg equation and Scherrer equation. The interlayer spacing of the phase was calculated from the (002) diffraction peak to be 6.6 Å, indicating that the interlayer distance of the nanocrystals is expanded. According to the Scherrer equation,[18] the average crystallite thickness is approximately 7 nm, which equates to approximately ten layers of MoS_2. These findings corroborate the HRTEM results that the MoS_2@C nanofibers are composed of nanosheets. The expanded layers can afford more space for Li-ion intercalation, thus leading to an enhanced storage capacity. In addition, all the diffraction peaks are strong and narrow, and the noise peaks decrease after the annealing process, which attests to the good crystallinity of MNF450. Raman spectroscopy was utilized to identify the formation of MNF450 and MNF800. As shown in Figure S1 (Supporting Information), there are two peaks of MNF450, located at 378 and 405 cm^{-1}, which can be attributed to the vibrational mode of the S–Mo–S bond. However, the same vibrational mode of the S–Mo–S bond is shifted to a slightly lower value for MNF800. The narrow and strong peaks of MNF450 may be attributed to its better crystallinity and fewer defects, which is in good agreement with the XRD results. Consequently, MoS_2 nanofibers treated in a reduction atmosphere with a subsequent annealing process have good crystallinity and an improved electrochemical performance.

Figure 3a displays a TEM image of the mesoporous MoS_2@C nanofibers (MNF450). The fibers are about 150 nm in diameter, and corn-like MoS_2 nanocrystals are embedded in the mesoporous carbon fibers. It is clear that the corn-like MoS_2 nanocrystals are very small and are distributed homogeneously in the fibers. Upon closer observation, as shown in Figure 3b, it is found that the surface of the nanofibers is rough and uneven, and the MoS_2 nanocrystals are interconnected within the fibers. The morphology and size of the sample obtained from the TEM results match well with those observed from the SEM images. The uniform dispersion of MoS_2 nanocrystals in the carbon fibers (highlighted by the white square is further confirmed by HRTEM (shown in Figure 3c), which provides more detailed structural information. It is clear that the typical mesoporous MoS_2@C nanofibers are composed of ultrafine nanocrystals embedded in overlaying amorphous carbon as well as uniformly dispersed within the nanofibers. The nanocrystals are approximately 7 nm in thickness. A uniform thin carbon layer of about 2 nm is formed from the carbonization. The observed lattice spacing of the planes is 0.66 nm, which corresponds to the (002) plane of hexagonal MoS_2, slightly larger than the reported data (0.615 nm), and is consistent with the XRD results (JCPDS: 00-037-1492). The diffraction ring pattern of SAED (shown in Figure 3d) indicates the polycrystalline nature of the MoS_2@C nanofibers. For determination of the weight ratio of MoS_2 to carbon, TGA was performed on the nanofibers from room temperature to 700 °C at a rate of 10 °C min^{-1} in air (Figure S2, Supporting Information). The large weight loss at 400 °C is attributed to the oxidation of MoS_2 to MoO_3 and the combustion of the carbon nanofibers.[19] The weight fraction of MoS_2 in the MoS_2@C nanofibers was estimated to be about 70% by assuming that the remaining product after TGA was pure MoO_3.

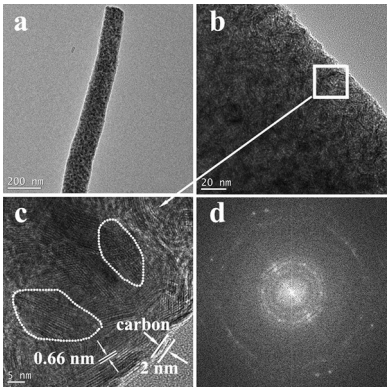

Figure 3. a) TEM image; b) HRTEM image of the MoS_2 nanocrystals embedded in the carbon nanofiber; c) corresponding HRTEM images from the marked region in (b); d) corresponding FFT pattern.

The surface electronic state and chemical composition of mesoporous MoS_2@C nanofibers (MNF450) was analyzed using XPS. Figure 4a shows four characteristic peaks located at 531.9, 284.6, 162.5, and 229.4 eV, corresponding to O 1s, C 1s,

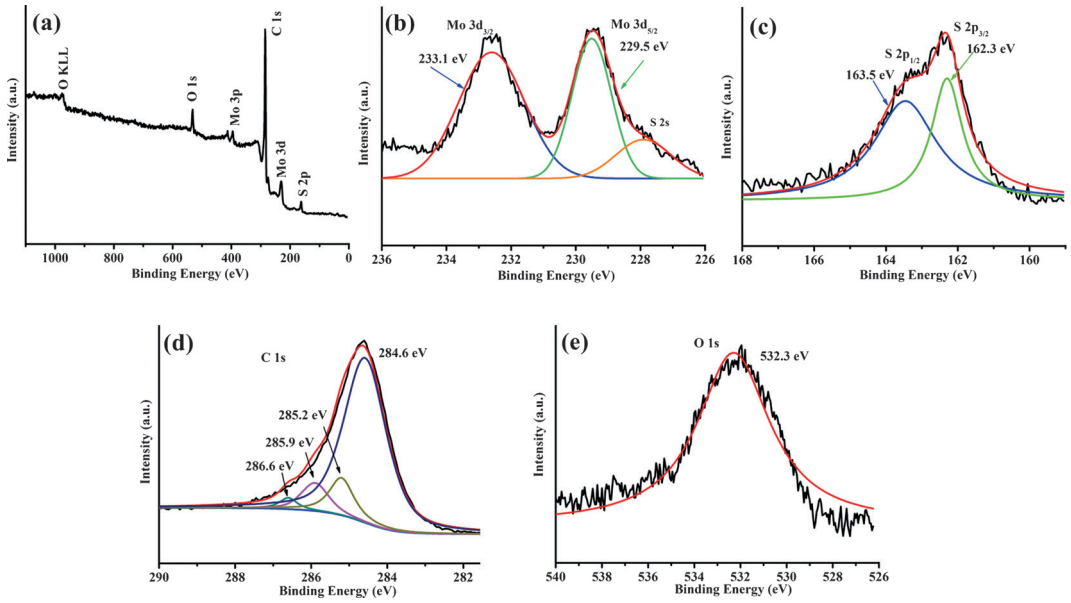

Figure 4. a) Wide-survey XPS spectrum of MNF450 nanofibers; the fine XPS of spectra b) Mo 3d; c) S 2p; d) C 1s; e) O 1s.

S 2p and Mo 3d. These results indicate that the sample contains Mo, S, C, and O elements. The locations of Mo $3d_{5/2}$, Mo $3d_{3/2}$, and S 2p in the survey spectrum can be indexed as MoS_2, which is highly consistent with the EDX results. The high-resolution scans shown in Figure 4b emphasized the spectrum of Mo 3d, in which the peaks located at 233.1 and 229.5 eV are indicative of doublet Mo $3d_{3/2}$ and Mo $3d_{5/2}$. The chemical valence in MoS_2 is confirmed as Mo^{4+}. The peak binding energies of S 2p shown in Figure 4c are162.3 and 163.5 eV, corresponding to the S $2p_{3/2}$ and S $2p_{1/2}$ orbitals, which can be indexed as S^{2-}. These surveys are in good agreement with literature reports for MoS_2.[20] The XPS spectrum of C 1s shows a strong peak at 284.6 eV (Figure 4d), which is assigned to the C–C bonds, indicating the formation of carbon nanofibers, whereas the weak ones located at 285.2, 285.9, and 286.6 eV correspond to carbon in phenolic groups, carbon in sp^3 groups such as C–O–H or C–O–C, and carbon in absorbed CO or CO_2, respectively.[21] These results confirm that the MoS_2 nanocrystals are formed after pyrolysis and the PVA is totally carbonized, demonstrating that the MoS_2 nanocrystals are encapsulated successfully in the carbon nanofibers. The strong O 1s peak at 532.3 eV indicates the presence of oxygen-containing groups such as C–O–H or C–O–C in the carbon nanofibers.

The N_2 adsorption/desorption isotherms for the mesoporous MoS_2@C nanofibers are shown in Figure S3 (Supporting Information) and the corresponding pore size distribution of the mesoporous materials was calculated using the BJH method (shown in Figure S4). The nitrogen sorption data for MNF800 and MNF450 are summarized in Table S1, including the surface area, and pore size distribution of mesopores and micropores. The BET-derived surface area of MNF450 is 135.9 $m^2 g^{-1}$, which is much larger than that of MNF800 (82.1 $m^2 g^{-1}$). Also, the surface area is superior to other MoS_2 nanomaterials obtained through hard-template or hydrothermal methods.[22] Furthermore, the average size of the mesopores increases from 3.3 to 3.7 nm. The annealing process is necessary to remove undesired functional groups and to open up the porous structure. The results confirm that the controlled heat treatment is a key factor affecting the microstructure. The nanofibers with porous feature would have more active openings that provide a large contact area between electrode and electrolyte, allowing fast electrolyte transport.

The electrochemical properties of the mesoporous MoS_2@C nanofibers were evaluated as the anode electrode for Li-ion batteries assembled in a half-cell configuration. Figure 5 shows the 1st, 2nd, and 5th cyclic voltammetry (CV) curves of the MNF800 and MNF450, respectively, obtained at a scan rate of 0.2 mV s^{-1} between 0.01and 3 V. Both samples appear to have similar CV curves, which explain their identical electrochemical reaction characteristics. For MNF800, in the initial cathodic sweep, there are two clear peaks located at 1.12 and 0.45 V (Figure 5a). The first peak can be assigned to the formation of Li_xMoS_2 accompanied by Li-ion intercalation into MoS_2.[23] The second peak is very intense, and corresponds to the conversion of MoS_2 to Mo nanoparticles embedded in a Li_2S matrix.[24] A gel-like SEI layer is formed owing to the electrochemical reaction occurring at the interface between the electrode and electrolyte. In the reverse anodic sweep, there is a pronounced peak at 2.25 V, which can be attributed to the extraction of Li_2S and oxidation of Mo to MoS_2. During the subsequent cycles, it is worth noting that the 0.45 V peak disappears, and the 1.12 V peak shifts to 1.22 V. In addition, a new reduction peak appears at 1.91 V. The electrode can be considered as a mixture of Mo and S rather than the original MoS_2. Accordingly, the two reduction peaks at 1.22 and 1.91 V can be attributed to the stepwise conversion reaction from S to Li_2S, which includes the reduction of sulfur to intermediate lithium polysulfides, and the reduction of higher-order polysulfides to Li_2S.[10b,25] In the fifth cycle, the anodic peak moves gradually to higher voltage, which indicates a gap between the redox

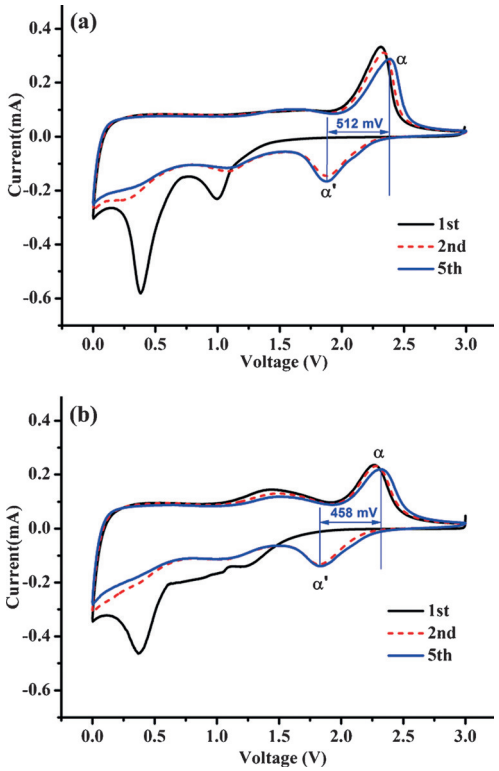

Figure 5. CV curves of a) MNF800, b) MNF450 measured in the voltage range 0.01–3.0 V at a scan rate of 0.2 mV s^{-1}.

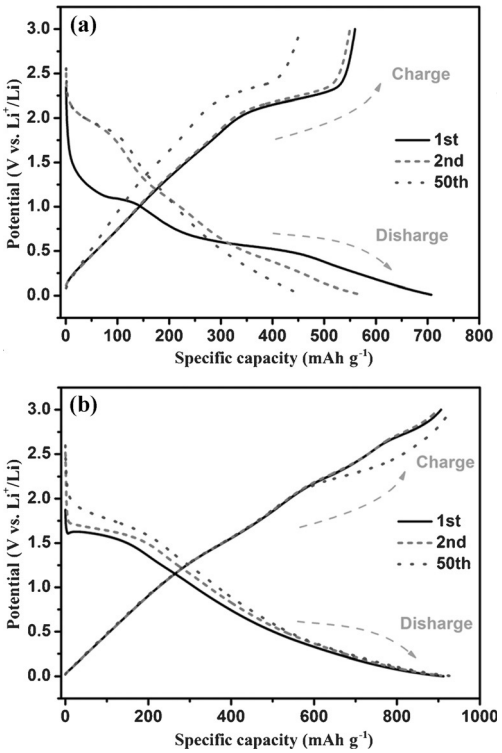

Figure 6. 1st, 2nd, and 50th discharge and charge curves of the samples a) MNF800 and b) MNF450 at a current density of 100 mA g^{-1}.

couple. The decrease in peak intensity of the redox couple indicates that an irreversible reaction takes place during the charge/discharge process. Overall, the CV curves of MNF800 overlap well except for a slight degradation, which means a capacity loss from the second cycle. Upon close examination, the CV curves of MNF450 (Figure 5b) were found to be slightly different from those of MNF800. According to the calculations, the potential difference of the redox couple α/α' of MNF450 is clearly smaller than that of MNF800 after five cycles. Specifically, the potential differences of the redox couples at α/α' of MNF450 and MNF800 are 458 and 512 mV, respectively. The smaller the potential difference in the redox couple, the more reversible the reaction taking place.[26] The first cathodic peak became ambiguous and narrow. This result may indicate that the Li ions not only intercalate into the MoS_2 layers, but are also located in the interface of the electrode because of the porous structure of the nanofibers. The cathodic and anodic peaks located at around 0.45 and 2.25 V correspond to the conversion reaction $MoS_2 + 4\,Li^+ + 4e^- \rightarrow Mo + 2\,Li_2S$. Similarly to MNF800, there is a small narrow peak located at 1.48 V, which can be attributed to the partial oxidation of Mo.[27] In the subsequent cycles, the cathodic peak at 0.45 V is absent, and two peaks at 1.01 and 1.86 V are observed. These peaks remain almost unchanged and steady, suggesting a highly reversible reaction and excellent stability of the MNF450 during the Li-ion insertion/extraction process. Accordingly, MNF450 shows better kinetics for Li-ion insertion/extraction.

Figure 6 shows the discharge and charge curves of MNF800 and MNF450 for the 1st, 2nd, and 50th cycles at a current density of 100 mA g^{-1} between 0.01 and 3.0 V. MNF800 exhibits initial discharge and charge capacities of 710 and 573 mA h g^{-1}, respectively. The discharge and charge capacity loss of 19.3% is attributed mainly to the formation of an SEI film and the irreversible side reaction between the electrolyte and electrode. There are two clear potential plateaus at 1.1 and 0.5 V in the discharging process and one potential plateau at 2.1 V in the charging process, which are in good agreement with those observed in the CV profiles. In the 2nd cycle, the discharge and charge capacities decrease to 591 and 568 mA h g^{-1}, respectively, and the reduction potential plateau moves to 1.97 V from 1.1 V in the initial cycles. The capacity experiences a sharp decay after 50 cycles and retains 64.8% of the initial discharge capacity. These results indicate that the capacity loss is related to the formation of a passivation film, which may block some active openings and reduce the effective contact area between the electrode and electrolyte. In comparison with MNF800, the MNF450 electrode delivers high initial discharge/charge capacities of 953 and 968 mA h g^{-1} with only 1.5% capacity loss. After the initial cycle, MNF450 exhibits monotonous charge and discharge profiles with a potential plateau at 1.81 V, indicating that Li ions are intercalated randomly between nanofibers without the formation of a stage structure like in the MNF800 electrodes. The charge and discharge potential curves overlap very well, explaining the good reversible reaction during Li-ion insertion/extraction. The discharge/charge capacities of 961 and 965 mA h g^{-1} are achieved, and the potential plateaus of the redox couple are closer after 50 cycles, which confirms the results obtained from the CV pro-

files. The capacity retention can be as high as 99.5% of that in the first cycle, demonstrating excellent stability, which is ascribed to the robust skeleton and mesoporous structure of the nanofibers.

Figure 7 compares the electrochemical performances of MNF800 and MNF450. The cycling performances of MNF800 and MNF450 at 0.5 A g^{-1} are shown in Figure 7a. It is evident that the two electrodes can obtain good capacity retention and highly reversible Li-ion storage capability after 200 cycles. Specifically, the MNF450 electrode has a higher specific capacity of 460 mA h g^{-1} with 13% capacity loss, whereas the corresponding values for MNF800 are 342 mA h g^{-1} with 35% capacity loss. At the same time, the two electrodes were tested under a current density of 1 A g^{-1} for 200 cycles (shown in the inset of the Figure 7a). The MNF450 electrode retains 71% more of the 10th capacity than the MNF800 electrode, indicating the good capacity retention and excellent Li-ion storage capability of the MNF450 electrode. These results are relatively competitive compared with previous reports.[28] The improved cycling stability under relatively high current density shows that the nanofibers with mesoporous microstructure and good crystallinity can achieve a good diffusion rate, which dominates the overall reaction rate, leading to fast charge-transfer kinetics.[15] These findings are further confirmed by the EIS results. Figure 7b shows the AC impedance spectroscopy measurements on a newly assembled cell of MNF450 and the data collected after 200 cycles. It is clear from the inset for R_{ct} (charge transfer resistance) that the MNF450 electrode exhibits a much lower charge-transfer resistance (148 Ω) than that of the fresh cell (385 Ω). The resistance of the MNF450 electrode after 200 cycles decreased by more than a half, indicating that the porosity of the nanofibers may facilitate charge transfer between the electrode and electrolyte interface, which may be helpful in reducing polarization. Hence, the interfacial charge-transfer reaction may be the rate-determining step for the high diffusional flux of Li ions in the host nanofibers.[15]

The rate capabilities at various current densities and cycling performances of the mesoporous MoS_2@C nanofiber electrodes were measured after 50 cycles at 0.1 A g^{-1}, and the results for MNF450 and MNF800 were compared. Figure 7c shows a comparison of the rate capability behavior from 0.1 to 5 A g^{-1} in the voltage range 0.01–3.0 V. Notably, these two electrodes have much closer specific capacities with increasing current rates. Unlike the data collected at the higher current rates, both the electrodes can recover to their original capacity values after 50 cycles at a current density of 0.1 A g^{-1}. Specifically, the MNF450 electrode can deliver discharge capacities of 1330, 1035, 788, 584, 396, and 196 mA h g^{-1} at rates of 0.1, 0.2,

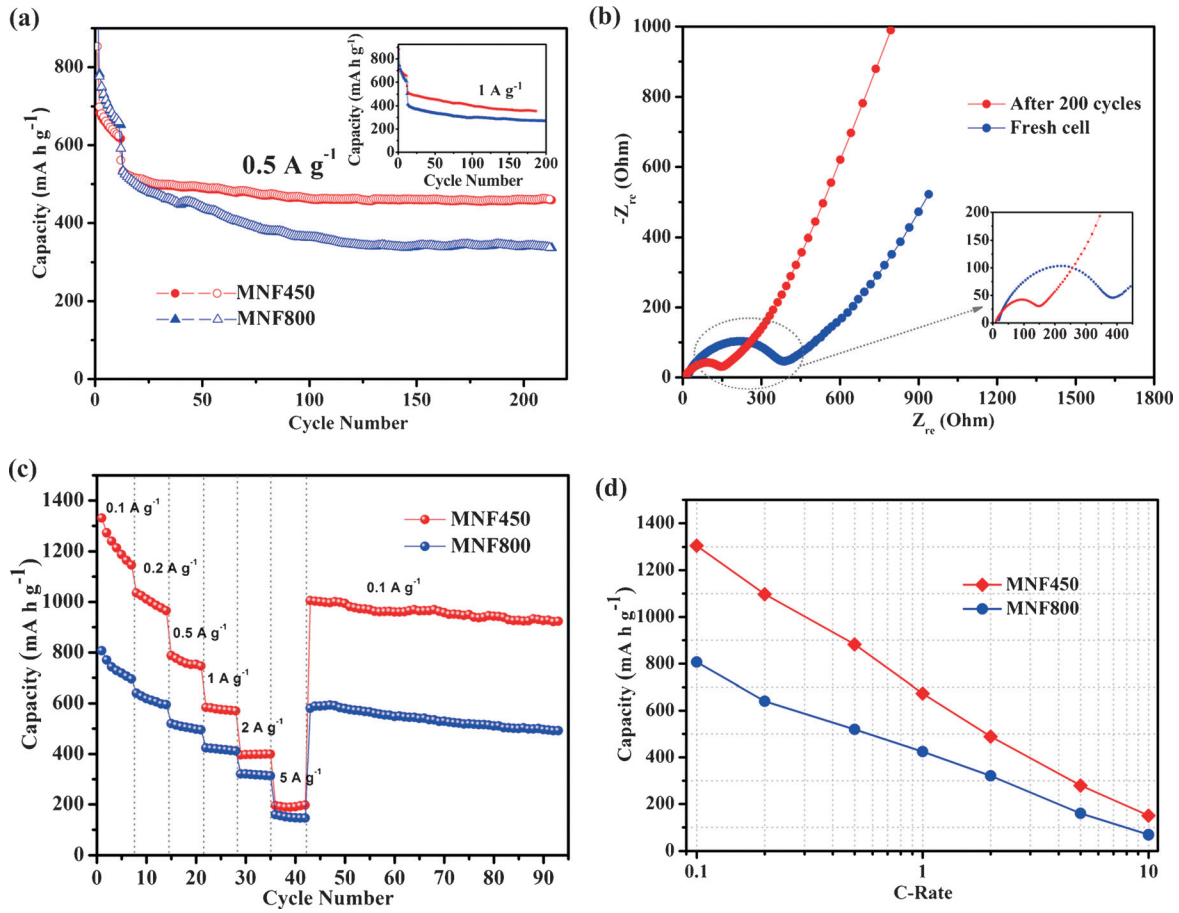

Figure 7. Comparison of electrochemical properties of MNF800 and MNF450: a) Cycling performances at scan rates of 0.5 A g^{-1} and 1 A g^{-1}; b) Nyquist plots; c) rate and cycling performances at various current densities; d) rate capacity retention.

0.5, 1, 2, and 5 A g^{-1}, respectively. The MNF800 electrode maintains discharge capacities of only 807, 640, 520, 424, 320, and 160 mA h g^{-1} at the same rates. After the current rates changed back to 0.1 A g^{-1}, the discharge capacity of the MNF450 electrode could recover to 1006 mA h g^{-1} with only 7.7% capacity loss throughout the cycling process, which increased to the ends of the cycling. However, the MNF800 electrode experienced a drop in capacity after the current rates changed back to normal, with the capacity then stabilizing at 493 mA h g^{-1} after 50 cycles. The MNF450 electrode has a high rate capacity, double that of its counterpart, which can be attributed to the following reasons. First, the porosity of MNF450, which leads to a large surface area of the nanofibers, indicates an increased contact area between the electrode and electrolyte. Secondly, the annealing conditions also play a key role in determining the crystallinity and mesoporous microstructure of the nanofibers, which may affect the Li-ion intercalation within the nanofiber anode. In summary, the disparity between MNF450 and MNF800 in terms of rate capability is associated with the diffusion rate in the nanofiber electrodes, which may decide the overall reaction rate. A comparison of rate capacity retention of the MNF450 and MNF800 electrodes is shown in Figure 7d. It is clear that the MNF450 results are all greater than those for MNF800. At the lower current rates in particular, the capacity of MNF450 is nearly twice that of MNF800. Despite the small differences between these two electrodes, the MNF450 electrode can deliver 204 mA h g^{-1} at a high current rate of 10 A g^{-1}. The good rate retention can be ascribed to the better crystallinity of the nanofibers, which affects the diffusion behavior of Li ions, and the fast interfacial charge-transfer reaction of the carbon nanofibers is improved by embedding MoS_2 within the mesoporous nanofibers. More importantly, the oxygen mass fraction in MNF450 is smaller than that in MNF800, which is a key factor influencing the electrochemical performance. The small amount of oxygen leads to better crystallinity, which brings about a lower internal resistance, thus improving the conductivity of MNF450.

The cycling stability and Coulombic efficiency of MNF450 were evaluated at a current density of 100 mA g^{-1} (Figure 8). The initial charge and discharge capacities are 1005 and 1022 mA h g^{-1}, respectively. The MNF450 electrode exhibits excellent cycling stability in spite of a capacity loss during the midway charge/discharge process, which may be attributed to the decreased ionic diffusion or the passive film formed at the interface of the electrode. After 165 cycles, a reversible capacity of 995 mA h g^{-1} can be retained, corresponding to 97.4% of the initial discharge capacity. The Coulombic efficiency of the MNF450 electrode approaches nearly 100%, indicating exceptional reversible capacity retention. To our knowledge, the theoretical capacity of graphite is 372 mA h g^{-1}. The capacity of the MNF450 electrode is almost twice that of graphite anodes, indicating an alternative for the high-capacity anodes in practical cells.

As expected, the mesoporous MoS_2@C nanofibers exhibit an extraordinary reversible capacity and long-term cycling stability. This can be explained by the following factors. The improvement in the electrochemical performance can be understood by considering a simple model made to depict how the mesoporous MoS_2@C nanofibers favor the Li-ion storage (shown in Figure 9). First, the nanofibers provide a robust and free-standing framework, which retains the structural integrity to circumvent the volume variation of the electrode. This feature guarantees a reversible reaction upon Li-ion insertion/extraction during cycling. Secondly, the carbon nanofibers act as an adaptable overcoat, which is able to deform synchronously during the volume change of the nanofibers rather than becoming cracked. In addition, the carbon nanofibers improve the conductivity of the overall electrode, thus contributing to the total capacity. Thirdly, the MoS_2@C nanofibers possess superior crystallinity and mesoporous characteristics, which allow sufficient penetration of the electrolyte into the electrode, and thus, facilitate the diffusional flux of Li ions and the interfacial charge-transfer reaction at high current rates. In addition, the increased surface areas provide efficient contact areas between the electrodes and electrolyte. Furthermore, the more active openings reduce the diffusion barrier for the Li ions to cross, leading to a high rate capability. The ultrasmall nanosized MoS_2 serves as a shortened lateral contact between the nanocrystals and carbon nanofibers, which is beneficial for the fast diffusion of Li ions and electrons. Finally, the small amount of oxygen leads to a better crystallinity, which brings about a lower internal resistance, and thus, improves the conductivity. These advantageous features of the nanofibers can contribute to their enhanced electrochemical performance for high-performance Li-ion battery applications.

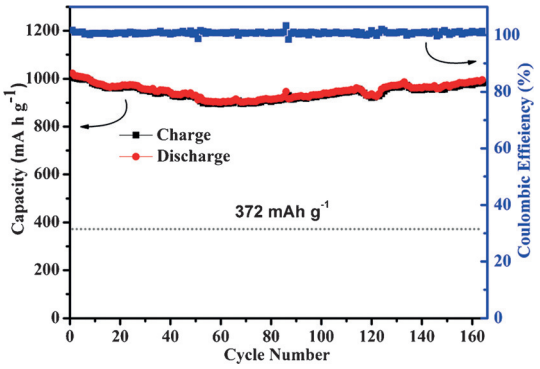

Figure 8. Cycling stability and Coulombic efficiency of MNF450 at a current density of 100 mA g^{-1} compared with the theoretical capacity of graphite.

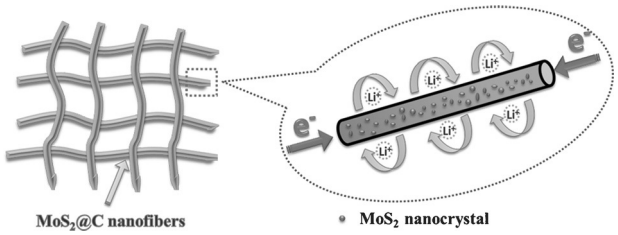

Figure 9. Schematic diagram of the mesoporous MoS_2@C nanofiber electrode.

4. Conclusion

A simple electrospinning method with subsequent calcination has been demonstrated for the successful fabrication of corn-like MoS_2 nanocrystals embedded into mesoporous carbon nanofibers. With controlled heat treatment, MoS_2 nanocrystals were obtained with smaller diameter ($\approx$7 nm) and expanded interlayers ($\approx$0.66 nm), which are favorable for fast Li-ion transport during cycling. The thin amorphous carbon overcoat is the backbone of the as-synthesized nanofibers, which not only guarantees structural integrity but also affords a conductive framework, thus contributing to the Li-ion storage capability. The better crystallinity and mesoporous microstructure of the MoS_2@C nanofibers lead to an increased surface area, giving sufficient contact areas between electrodes and electrolyte, as well as facilitating diffusion within the electrode. The small amount of oxygen in the nanofibers annealed in H_2 contributes to their lower internal resistance, which is favorable for enhanced conductivity. Considering all these advantages, the mesoporous MoS_2@C nanofibers can deliver a remarkable reversible capacity of 1022 mA h g^{-1} with only 2.3% capacity loss at a current density of 100 mA g^{-1}after 165 cycles, and retain an improved long cycling stability at a high current rate (1 A g^{-1}) upon assembly as an anode material for the Li-ion battery. According to these results, the extraordinary Li-ion storage capability of the mesoporous MoS_2@C nanofibers can be attributed to the synergetic effect between the ultrafine MoS_2 nanocrystals and the carbon nanofibers, with an increased surface area and superior crystallinity and porosity features. Such high-performance nanofiber electrodes fabricated through the simple, low-cost electrospinning process would be commercially viable for the mass production of Li-ion batteries.

Acknowledgements

This work was supported by the International Science & Technology Cooperation Program of China (No. 2013DFR50710), the National Natural Science Foundation of China (No. 51202174), the Equipment Pre-research Project (No. 625010402), the Science and Technology Support Program of Hubei Province (No. 2014BAA096), and the National Nature Science Foundation of Hubei Province (No. 2014CFB165). Shan Hu also appreciates the scholarship for Ph.D. study from the China Scholarship Council (CSC) at the University of Washington.

Keywords: anodes · carbon nanofibers · electrospinning · lithium-ion batteries · mesoporous materials · nanostructures · MoS_2

[1] a) B. Dunn, H. Kamath, J. M. Tarascon, *Science* **2011**, *334*, 928–935; b) V. Etacheri, R. Marom, R. Elazari, G. Salitra, D. Aurbach, *Energy Environ. Sci.* **2011**, *4*, 3243–3262.

[2] a) F. Cheng, J. Liang, Z. Tao, J. Chen, *Adv. Mater.* **2011**, *23*, 1695–1715; b) M. Armand, J. M. Tarascon, *Nature* **2008**, *451*, 652–657; c) B. Kang, G. Ceder, *Nature* **2009**, *458*, 190–193.

[3] a) A. S. Aricò, P. Bruce, B. Scrosati, J. M. Tarascon, W. Van Schalkwijk, *Nat. Mater.* **2005**, *4*, 366–377; b) C. Jiang, E. Hosono, H. Zhou, *Nano Today* **2006**, *1*, 28–33; c) Q. Zhang, E. Uchaker, S. L. Candelaria, G. Cao, *Chem. Soc. Rev.* **2013**, *42*, 3127–3171; d) S. Hu, F. Yin, E. Uchaker, M. Zhang, W. Chen, J. Zhou, Y. Qi, G. Cao, *J. Phys. Chem. C* **2014**, *118*, 24890–24897; e) J. Qian, W. A. Henderson, W. Xu, P. Bhattacharya, M. Engelhard, O. Borodin, J.-G. Zhang, *Nat. Commun.* **2015**, *6*, 6362–7362.

[4] a) S. Lee, J. Ha, J. Choi, T. Song, J. W. Lee, U. Paik, *ACS Appl. Mater. Interfaces* **2013**, *5*, 11525–11529; b) Y. Wang, H. Li, P. He, E. Hosono, H. Zhou, *Nanoscale* **2010**, *2*, 1294–1305.

[5] D. Yu, C. Chen, S. Xie, Y. Liu, K. Park, X. Zhou, Q. Zhang, J. Li, G. Cao, *Energy Environ. Sci.* **2011**, *4*, 858–861.

[6] Y. Tang, D. Wu, S. Chen, F. Zhang, J. Jia, X. Feng, *Energy Environ. Sci.* **2013**, *6*, 2447–2451.

[7] L. Shen, X. Zhang, E. Uchaker, C. Yuan, G. Cao, *Adv. Energy Mater.* **2012**, *2*, 691–698.

[8] a) Y. Shi, B. Guo, S. A. Corr, Q. Shi, Y. Hu, K. R. Heier, L. Chen, R. Seshadri, G. D. Stucky, *Nano Lett.* **2009**, *9*, 4215–4220; b) C. Yuan, J. Li, L. Hou, X. Zhang, L. Shen, X. W. D. Lou, *Adv. Funct. Mater.* **2012**, *22*, 4592–4597; c) Q. Hao, S. Liu, X. Yin, Z. Du, M. Zhang, L. Li, Y. Wang, T. Wang, Q. Li, *CrystEngComm* **2011**, *13*, 806–812; d) Z. Jian, X. Lu, Z. Fang, Y.-S. Hu, J. Zhou, W. Chen, L. Chen, *Electrochem. Commun.* **2011**, *13*, 1127–1130.

[9] a) R. Ostermann, D. Li, Y. Yin, J. T. McCann, Y. Xia, *Nano Lett.* **2006**, *6*, 1297–1302; b) N. Zhu, W. Liu, M. Xue, Z. Xie, D. Zhao, M. Zhang, J. Chen, T. Cao, *Electrochim. Acta* **2010**, *55*, 5813–5818.

[10] a) S. Hu, W. Chen, J. Zhou, F. Yin, E. Uchaker, Q. Zhang, G. Cao, *J. Mater. Chem. A* **2014**, *2*, 7862–7872; b) T. Stephenson, Z. Li, B. Olsen, D. Mitlin, *Energy Environ. Sci.* **2014**, *7*, 209–231.

[11] a) H. Li, W. Li, L. Ma, W. Chen, J. Wang, *J. Alloys Compd.* **2009**, *471*, 442–447; b) H. Hwang, H. Kim, J. Cho, *Nano Lett.* **2011**, *11*, 4826–4830; c) C. Zhang, Z. Wang, Z. Guo, X. W. Lou, *ACS Appl. Mater. Interfaces* **2012**, *4*, 3765–3768; d) C. Zhang, H. B. Wu, Z. Guo, X. W. D. Lou, *Electrochem. Commun.* **2012**, *20*, 7–10.

[12] a) K. Chang, W. Chen, *J. Mater. Chem.* **2011**, *21*, 17175–17184; b) L. Yang, S. Wang, J. Mao, J. Deng, Q. Gao, Y. Tang, O. G. Schmidt, *Adv. Mater.* **2013**, *25*, 1180–1184; c) J. Z. Wang, L. Lu, M. Lotya, J. N. Coleman, S. L. Chou, H. K. Liu, A. I. Minett, J. Chen, *Adv. Energy Mater.* **2013**, *3*, 798–805; d) X. Zhou, L.-J. Wan, Y.-G. Guo, *Chem. Commun.* **2013**, *49*, 1838–1840; e) X. Zhou, L. Wan, Y. Guo, *Nanoscale* **2012**, *4*, 5868–5871; f) X. Y. Yu, H. Hu, Y. Wang, H. Chen, X. W. D. Lou, *Angew. Chem. Int. Ed.* **2015**, *54*, 7395–7398; *Angew. Chem.* **2015**, *127*, 7503–7506.

[13] C. Zhu, X. Mu, P. A. van Aken, Y. Yu, J. Maier, *Angew. Chem. Int. Ed.* **2014**, *53*, 2152–2156; *Angew. Chem.* **2014**, *126*, 2184–2188.

[14] C. Zhao, J. Kong, X. Yao, X. Tang, Y. Dong, S. L. Phua, X. Lu, *ACS Appl. Mater. Interfaces* **2014**, *6*, 6392–6398.

[15] W. van Schalkwijk, B. Scrosati, *Advances in Lithium-Ion Batteries*, Springer, New York, **2002**.

[16] M. Zhang, E. Uchaker, S. Hu, Q. Zhang, T. Wang, G. Cao, J. Li, *Nanoscale* **2013**, *5*, 12342–12349.

[17] S. Liu, X. Zhang, H. Shao, J. Xu, F. Chen, Y. Feng, *Mater. Lett.* **2012**, *73*, 223–225.

[18] V. Drits, J. Srodon, D. Eberl, *Clays Clay Miner.* **1997**, *45*, 461–475.

[19] a) X. Xu, Z. Fan, X. Yu, S. Ding, D. Yu, X. W. D. Lou, *Adv. Energy Mater.* **2014**, *4*, 1400902, doi: 10.1002/aenm.201400902; b) Y. Wang, G. Xing, Z. Han, Y. Shi, J. I. Wong, Z. X. Huang, K. Ostrikov, H. Yang, *Nanoscale* **2014**, *6*, 8884–8890.

[20] a) K. K. Liu, W. Zhang, Y. H. Lee, Y. C. Lin, M. T. Chang, C. Y. Su, C. S. Chang, H. Li, Y. Shi, H. Zhang, *Nano Lett.* **2012**, *12*, 1538–1544; b) C. Altavilla, M. Sarno, P. Ciambelli, *Chem. Mater.* **2011**, *23*, 3879–3885; c) X. L. Li, Y. D. Li, *J. Phys. Chem. B* **2004**, *108*, 13893–13900.

[21] a) H. Zhu, F. Lyu, M. Du, M. Zhang, Q. Wang, J. Yao, B. Guo, *ACS Appl. Mater. Interfaces* **2014**, *6*, 22126–22137; b) K. Palanisamy, Y. Kim, H. Kim, J. M. Kim, W.-S. Yoon, *J. Power Sources* **2015**, *275*, 351–361.

[22] a) X. Fang, X. Yu, S. Liao, Y. Shi, Y. S. Hu, Z. Wang, G. D. Stucky, L. Chen, *Microporous Mesoporous Mater.* **2012**, *151*, 418–423; b) H. Liu, D. Su, R. Zhou, B. Sun, G. Wang, S. Z. Qiao, *Adv. Energy Mater.* **2012**, *2*, 970–975.

[23] a) L. Zhang, H. B. Wu, Y. Yan, X. Wang, X. W. D. Lou, *Energy Environ. Sci.* **2014**, *7*, 3302–3306; b) E. Benavente, M. Santa Ana, F. Mendizábal, G. González, *Coord. Chem. Rev.* **2002**, *224*, 87–109.

[24] a) G. Du, Z. Guo, S. Wang, R. Zeng, Z. Chen, H. Liu, *Chem. Commun.* **2010**, *46*, 1106 – 1108; b) J. Xiao, D. Choi, L. Cosimbescu, P. Koech, J. Liu, J. P. Lemmon, *Chem. Mater.* **2010**, *22*, 4522 – 4524.

[25] a) X. Fang, X. Guo, Y. Mao, C. Hua, L. Shen, Y. Hu, Z. Wang, F. Wu, L. Chen, *Chem. Asian J.* **2012**, *7*, 1013 – 1017; b) J. Xiao, X. Wang, X. Q. Yang, S. Xun, G. Liu, P. K. Koech, J. Liu, J. P. Lemmon, *Adv. Funct. Mater.* **2011**, *21*, 2840 – 2846.

[26] Y. Li, J. Yao, E. Uchaker, M. Zhang, J. Tian, X. Liu, G. Cao, *J. Phys. Chem. C* **2013**, *117*, 23507 – 23514.

[27] F. Zhou, S. Xin, H. W. Liang, L. T. Song, S. H. Yu, *Angew. Chem. Int. Ed.* **2014**, *53*, 11552 – 11556; *Angew. Chem.* **2014**, *126*, 11736 – 11740.

[28] a) Z. Wang, T. Chen, W. Chen, K. Chang, L. Ma, G. Huang, D. Chen, J. Y. Lee, *J. Mater. Chem. A* **2013**, *1*, 2202 – 2210; b) L. Zhang, X. W. D. Lou, *Chem. Eur. J.* **2014**, *20*, 5219 – 5223; c) Z. Wan, J. Shao, J. Yun, H. Zheng, T. Gao, M. Shen, Q. Qu, H. Zheng, *Small* **2014**, *10*, 4975 – 4981.

Received: August 24, 2015
Published online on October 30, 2015